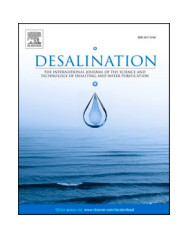


Contents lists available at ScienceDirect

Desalination

journal homepage: www.elsevier.com/locate/desal





Carbonized cattle manure-based photothermal evaporator with hierarchically bimodal pores for solar desalination in high-salinity brines

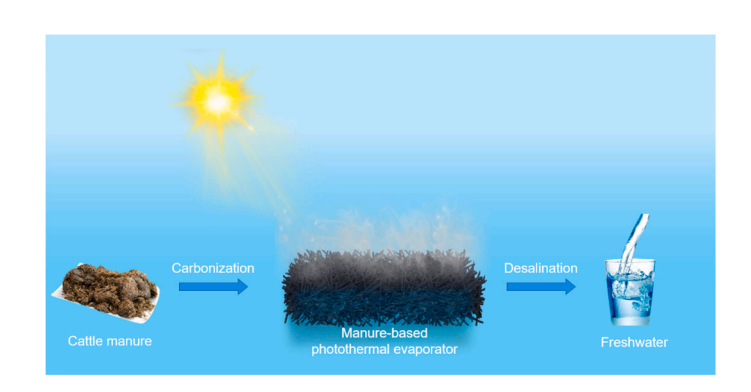
Yanpei Tian^a, Xiaojie Liu^a, Ziqi Wang^a, Andrew Caratenuto^a, Fangqi Chen^a, Yinsheng Wan^b, Yi Zheng^{a,*}

- ^a Department of Mechanical and Industrial Engineering, Northeastern University, Boston, MA 02115, USA
- ^b Department of Biology, Providence College, Providence, RI 02918, USA

HIGHLIGHTS

- A manure-based porous carbon foam for high-salinity interfacial solar desalination
- Achieve an evaporation rate of 2.25 kg m⁻² h⁻¹ in 15 wt% NaCl solution under
- Randomly arranged carbon fibers forming hierarchical channels for solar absorptance
- A carbon foam stability works in 20 wt% brine without salt accumulations.

GRAPHICAL ABSTRACT



ARTICLE INFO

Keywords:
Biomass
Solar desalination
Manure
Farm waste
High salinity

ABSTRACT

Interfacial solar desalination shows great promise to become an alternative technique for freshwater generation. However, the unavoidable fouling undermines continuous evaporation because the accumulated salt crystals weaken sunlight absorption and salt drainage, especially in high-salinity brines. Therefore, developing a photothermal evaporator with excellent salt rejection capability is urgent for high-salinity solar desalination. Here, a carbonized cattle manure-based photothermal evaporator with hierarchically bimodal pores is validated as an efficient desalinator for high-salinity brine (≥ 15 wt%). Taking advantage of the bimodally porous structure and interconnected microchannels formed by carbon fiber networks, it realizes rapid water transportation and quickly replenishes the surface-desalinated brine to prevent salt accumulation and enable stable freshwater generation. This carbonized manure evaporation device demonstrates a rapid evaporation rate of 2.25 kg m $^{-2}$ h $^{-1}$ under 1 sun irradiance (1 kW m $^{-2}$) using a 15 wt% NaCl solution, as well as excellent long-term stability for the high-salinity desalination process. The nano-sized channels offer efficient nanoscale light trapping through multiple reflections and scatterations that occur within the channel walls. Furthermore, the abundance of raw materials provides a desirable and efficient approach for converting farm waste to energy, making it particularly well-suited for developing regions.

E-mail address: y.zheng@northeastern.edu (Y. Zheng).

^{*} Corresponding author.

1. Introduction

The ever-increasing freshwater scarcity is emerging as one of the most serious global challenges for human society due to the rapid expansion of civilization and frequent water pollution accidents, contributing respectively to substantially increased water consumption and contamination levels of freshwater [1,2,3]. Water desalination or purification from seawater and sewage is growing to be one of the most cost-effective approaches to increase freshwater availability [4,5,6]. Various desalination technologies, such as reverse osmosis (RO) [7,8] and multi-stage flash [9,10], have been demonstrated as mature and scalable implementations for yielding clean water. However, the features of high energy consumption, complicated and high-end infrastructure, and large installation occupation impede their deployment in off-grid regions and most underdeveloped countries [11,12]. Moreover, the energy consumption required to drive filtration processes in RO systems increases greatly with the growing operating pressure, resulting from the rise of the feed brine concentration [13,14]. The membrane lifespan in RO systems is also shortened significantly due to the fouling potential from salt accumulation [15]. The large amounts of highsalinity brine generated by the RO industry also have the potential to cause severe environmental and ecological harm to human communities and natural ecosystems. Therefore, it is essential to develop novel pathways for desalination that present few front-end investments and negligible environmental footprints.

Recently, solar-driven interfacial desalination has attracted intensive attention due to the abundance of solar energy and minimal environmental footprint, especially for off-grid regions lacking reliable electricity supplies [16,17,18,19,4]. For instance, cow dung cakes [20], blue metal stones [21], sandstones, marble pieces [22,23], and hybrid graphene/TiO2 nanoparticles [24,25] are investigated as thermal energy storage to enhance the distillate output. However, it is difficult to maintain the high evaporation rate because of the salt accumulation on the evaporation surface, particularly when applied to high-salinity brines [26,27,28,29]. The accumulated salt blocks the incident sunlight, affecting photothermal conversion, and plugs the interior salt drainage and water transportation path, causing dramatic degradation of the evaporation performance [30,16]. This salt clogging process resembles an "avalanche effect", resulting in more severe fouling as this process progresses, eventually leading to the collapse of desalination. Thus, minimizing salt accumulation in a solar desalination system is an important challenge to overcome in developing stable and highefficiency solar evaporation devices [31,32,33,34,35,36,37]. The salt accumulation issue servery hinders the continuous working of interfacial solar desalination, especially during which the water salinity is above 15 wt% since the high-salinity water supply even impedes the salt rejection process [38,39,40,41].

In the past few years, various strategies have been investigated for achieving a continuous evaporation rate in a high salinity brine. Kashyap et al. and Xu et al. designed hydrophobic interfaces to impede salt accumulation in the interfacial evaporation layer in a relatively lowsalinity environment [42,43]. Even though this design is effective in preventing salt accumulation, the heat dissipation to the bulk water due to the unsatisfactory thermal insulation between the evaporation surface and the underlying water hurts its evaporation performance. Furthermore, the high material cost is another key factor limiting scalable deployment in practical applications. Xu et al. demonstrated a hierarchical structure inspired by the water lily for high-salinity brine (10 wt %) and wastewater containing heavy metal ions (30 wt%), which forms a thin water layer sandwiched between the top hydrophobic absorber and the bottom stand [44]. He et al. proposed a surface-carbonized porous wood membrane using balsa wood as a starting material in the brine of 15 wt% [40]. Cheng et al. designed a lotus leaf-like vertical solar evaporator by assembling silicon/polypyrrole-polyvinyl alcohol sponge and multi-root columnar polyvinyl alcohol sponge and yielded a stable evaporation rate of 1.35 kg m⁻² h⁻¹ out of 26.6 wt% brine [45]. Chen

et al. fabricated a rice husk-based biomass hydrogel evaporator with rationally architected sponge-like skeletons and led to a long-term evaporation rate of 1.77 kg m $^{-2}$ h $^{-1}$ out of 25 wt% brine [46]. Despite the effectiveness in preventing salt from accumulating, the evaporation rate remains below 1.77 kg m $^{-2}$ h $^{-1}$ due to the sacrification of thermal insulation to achieve sufficient water supply for the sake of dissolving the accumulated salt. Therefore, it is challenging to achieve both continuous and efficient high-salinity desalination.

Herein, we demonstrate an effective salt-accumulation-free solar evaporation device derived from biomass-manure for continuous highsalinity desalination (>15 wt%) by a fully carbonized manure (CM) hierarchical porous structure (Fig. 1a). The manure is selected as a starting material due to its unique coexisting bimodal porous and interconnected microchannels, in which the larger channels range in diameter from 5 μ m to 30 μ m and the diameters of small channels range from 0.1 μ m to 1.5 μ m. Through the carbonization process of the cellulose fibers in manure, this material becomes an excellent photothermal material with a solar absorptance of 0.98, which is attributed to the multireflection and scatteration of the carbon fiber network (Fig. 1b). The porous structure of CM renders it a low thermal conductivity (0.15 W m⁻¹ K⁻¹) even after absorbing water, and effectively localizing heat within the small evaporation region, enabling interfacialtype solar evaporation (Fig. 1c). In the hierarchical porous structure of CM, the water diffusion and convection, enhanced by the strong capillary force within the carbon fibers contribute to rapid water transportation to the top evaporation surface (Fig. 1d). Simultaneously, the ample water supply capability also leads to the quick drainage of the evaporated brine downward to the bulk brine, preventing the salt from clogging the water supply channels and ensuring a continuous and efficient desalination process (Fig. 1e). Different from most of the previous studies for high-salinity solar-driven desalination which places the evaporator directly into the brine to ensure adequate water transportation and quick salt dissipation, the CM evaporation device consists of a top CM solar absorber and a bottom polystyrene (PS) foam thermal insulator. A hydrophilic cotton wipe serves as both the water pathway and salt drainage channel between the evaporator and the bulk brine. The PS foam prevents the direct heat dissipation from the CM evaporator to the bulk brine and increases the stable evaporation temperature of the CM evaporator. Solar evaporation is efficient since the absorbed solar energy is confined to the evaporator without dissipating downward. Another key factor is that the increased concentration of brine within the small channels can gradually diffuse to the surrounding large channels through the interconnected vessels, helping to avoid salt crystal formation on the evaporation surface. Therefore, this design can enable fast and stable desalination and demonstrates an evaporation rate of 2.25 kg m⁻² h⁻¹ under 1 sun irradiance (1 kW m⁻²) using the 15 wt% NaCl solution with outstanding stability and durability. No salt accumulation occurs even in the 20 wt% brine environment with an evaporation rate of 2.02 kg m⁻² h⁻¹. With unique hierarchical and interconnected porous structures fabricated by a scalable carbonization method and abundant biomass manure as raw material, our porous CM evaporator provides an attractive alternative for efficient, durable, costeffective, and environmentally-friendly solar desalination in highsalinity brines.

2. Experimental section

2.1. Materials

The cotton wipe employed as the water transportation path was purchased from Webril. The 13 mm thick PVC foam was provided by McMaster-Carr. NaCl (99.0%) was purchased from Sigma-Aldrich. The fresh manure was kindly provided by Blackbird Farm, Smithfield, RI, USA. 100 ml plastic beakers were purchased from Amazon.

2.2. CM evaporation device preparation

The collected fresh manure (45 g) was crushed into small pieces for molding using a high-speed blender for 3 min and hand-pressed into a cuboid (5 cm \times 5 cm \times 0.5 cm). The pressed manure cuboid was baked in a convection oven at 180 °C for 20 min, then carbonized in an argon atmospheric alumina cubic oven. The alumina cubic was connected to a rotary vane vacuum pump at one port and argon source at another port. The rotary van pump first vacuumed the cubic chamber down to $\hat{10}^{-2}$ Pa, then the argon input port was opened for 30 s to introduce argon and sweep air out. The vacuum/argon sweeping process was repeated three times to remove the air inside the cubic chamber. The baked manure cuboid was put in an alumina crucible boat and positioned in the center of the oven at 800 $^{\circ}\text{C}$ for 1 h. The carbonized manure foam was left to cool down to the ambient temperature in the argon environment (Fig. 2a). A 7 mm thick piece of PVC insulation foam was shaped into a circle with a diameter of 5.0 cm. The cotton wipe was cut into a piece measuring 5 cm \times 3 cm and was soaked into the bulk brine through a slit with a dimension of 3 cm \times 0.4 cm within the aforementioned PVC foam. The CM was placed on the soaked cotton wipe, and the water was pumped to the evaporation surface (Fig. 2b).

2.3. Solar-driven desalination experiments

Solar desalination experiments under different solar intensities were conducted by changing the output power of the power source in the solar simulator (Newport 94081a). The solar intensities (0.6, 0.8, 1.0, and 1.3 kW m $^{-2}$) were calibrated by a solar power meter (TES 132) before each experiment. The mass change of water was recorded by an electrical scale (RADWAG, PS 1000) with a resolution of 0.001 g at a frequency of 1 Hz. The mass change date of each experiment was selected from 0.5 h after the solar simulator was on to ensure that the evaporation rate was stable. The solar desalination experiments were conducted in a dark room with a temperature of $20.7{\sim}21.7~^{\circ}\text{C}$ and humidity of $50{\sim}52\%$.

2.4. Material characterizations

The reflectance spectra (0.3–2.5 μ m) were characterized by a Jasco V770 spectrophotometer using a Jasco ISN-923 integrating sphere. The FTIR transmittance spectra were measured by a Jasco FTIR 6600 spectrometer. The reflectance spectra for different angles of incidence were measured by employing wedges of different angles placed at the sample

port of the Jasco V770 spectrophotometer. The SEM images were characterized as Supra25 SEM at an acceleration voltage of 3 kV. Transmittance haze spectra are measured by following the procedure defined by Jasco [47]. The infrared images were recorded using the FLIR A655C thermal camera at a resolution of 640 \times 480. The thermal conductivity was measured by the Hotdisk TPS 2500 s using a standard module. The contact angle was measured by SINDIN SDC-350 contact angle meter. The XRD spectra were characterized by the Bruker D8 X-ray Diffractometer scanning from 15° to 100° with a stepsize of 0.02°. Highspeed images were recorded by the Chronos 2.1-HD. The optical profilometry images were scanned using a Bruker ContourGT-X8 optical profilometer. The solar intensity of the solar simulator was calibrated to be 0.5, 0.8, 1.0, and 1.3 kW m^{-2} using the TES 132 solar power meter before each experiment by changing the output of the power source. The salinity of the collected freshwater samples was measured by the Extech EC400 ExStik salinity meter.

2.5. Finite-difference time-domain (FDTD) simulation

FDTD simulation was conducted using Lumerical FDTD Solution 2020. Two-dimensional models were employed, and a total-field scattered field source coupled with scattering cross-sections of carbon fibers in different geometries (square, hexagon, triangular, and circle) was used to simulate the extinction coefficient over the wavelength of 0.3–2.5 μm . The characteristic size of cross-sections in different geometries is 10 μm to check the effects of various shapes on the scattering efficiency. The material of different geometries was set to be carbon and the refractive index of carbon was extracted from Palik's handbook [48]. The refractive index of air is 1.

3. Results and discussion

3.1. Fabrication and characterization of CM evaporator

Fig. 2a shows photographs of dry manure (left) and the CM evaporator (right) before being integrated into the final evaporation device. The manure changes from a dark brown color to an intense black color after a full carbonization treatment (Fig. S1). The CM has a thickness of 5.0 mm and can effectively absorb the incident sunlight, and converting solar energy into thermal energy for desalination. The hydrophilic cotton wipe can rapidly pump brine upward to the CM, and the hierarchical carbon fiber network subsequently transports brine to the top

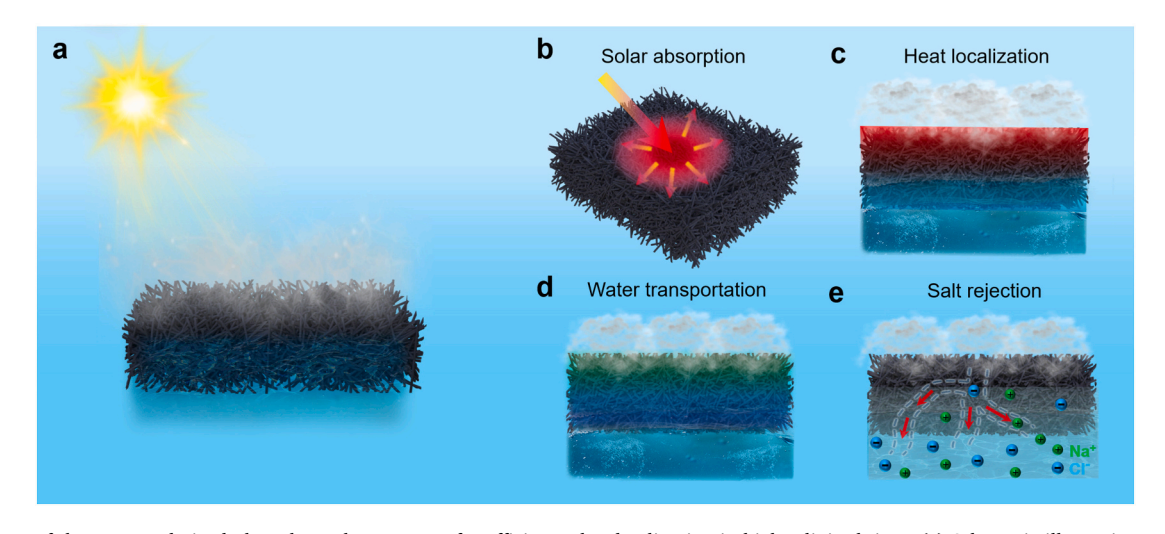


Fig. 1. Concept of the manure-derived photothermal evaporator for efficient solar desalination in high-salinity brines. (a) Schematic illustrations of the working mechanism of the CM evaporator. (b) The randomly organized carbon fibers form interconnected channels, serving as the black cavity, to capture the incident sunlight from different angles. (c) These randomly arranged carbon fibers contribute to the low thermal conductivity of CM and effectively localizing heat on the top evaporation region. (d) A strong capillary force arising from the microchannels architected by carbon fiber pumps to efficiently water the top evaporation interface. (e) Salt concentration gradients between the top evaporation surface and the bottom brine drive quick salt drainage through the interconnected microchannels in CM.

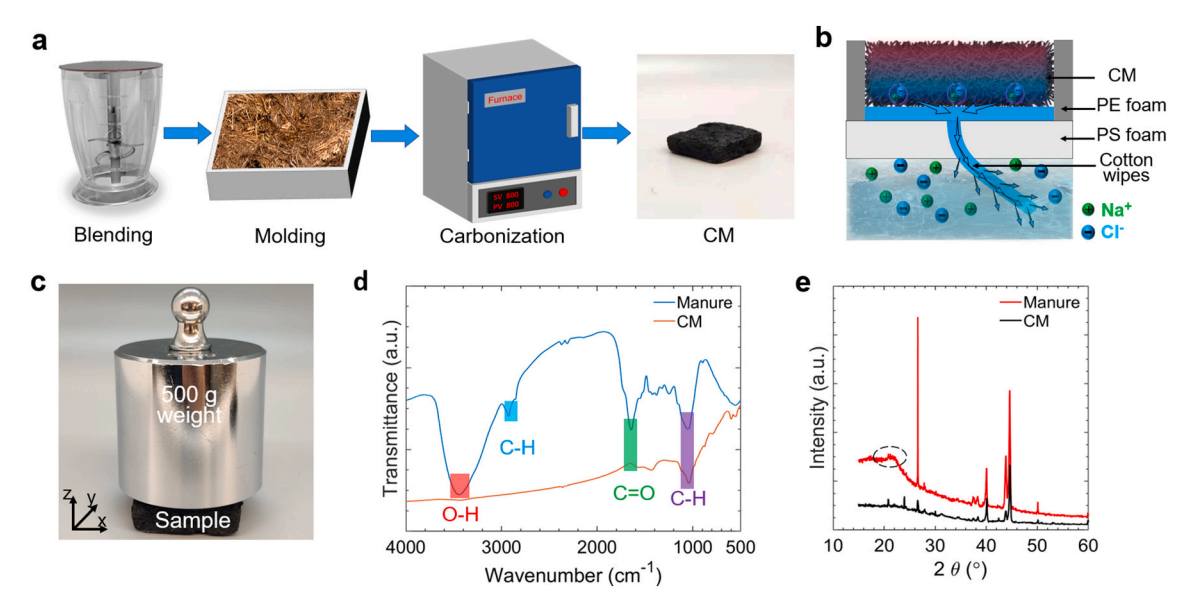


Fig. 2. Fabrication and characterizations of the CM. (a) The fabrication process of the CM evaporator. (b) Schematic showing the evaporation device for solar desalination. (c) Photograph elucidating the mechanical strength of the CM for real-world engineering applications. (d) FTIR and (e) XRD spectra of the dry manure and the CM.

evaporation region by capillary action (Fig. 2b). The evaporated brine becomes concentrated and dissipates through the vessel channels of the CM and cotton wipe to the bulk brine. This ensures continuous brine pumping and salt drainage without extra power input during the solar desalination process. CM is mechanically stable and can withstand over 330 times of its weight without cracking, ensuring scalable deployment for real-life applications (Fig. 2c). Analysis of the FTIR spectra elucidates that, at 800 °C carbonization temperature, the peaks of O–H stretching vibration at around 3500 cm⁻¹ and the C–H bond at 2920 cm⁻¹ disappear. The decreasing peak intensity of C=O bond at 1645 cm⁻¹ indicate the removal of the cellulose/hemicellulose above 800 °C (Fig. 3d). X-ray diffraction pattern indicates a broad peak (black dash circle, at 20°–25°) from the raw manure, which vanishes in CM treated at 800 °C due to the carbonization of cellulose into carbon (Fig. 2e).

Scanning electron microscope (SEM) images illustrate the structure of CM, which is in a hierarchical form consisting of \sim 5 μ m to 30 μ m

microchannels partitioned by nano-sized channels (Fig. 3a–d). Channel size measurements indicate that the size of the channel is bimodally distributed, with broad channels size distributions centering at $\sim\!0.3~\mu\mathrm{m}$ and $\sim\!10~\mu\mathrm{m}$ for the nano- and microchannels from the side view, respectively (Figs. 3a,b and S2). Similar distributions centering at $\sim\!0.7~\mu\mathrm{m}$ and $\sim\!5~\mu\mathrm{m}$ for the nano- and microchannels are also observed in the top view (Figs. 3c,d and S3). These nanochannels provide nanoscale light trapping for efficient solar absorption, while the microstructure provides pathways for water transportation and salt drainage. These microstructural configurations are essential for the CM evaporator to avoid salt accumulation and allow for sufficient water transportation during the desalination process.

3.2. Solar and water absorption behaviors of CM evaporator

One of the key aspects critical to achieving a high solar-driven

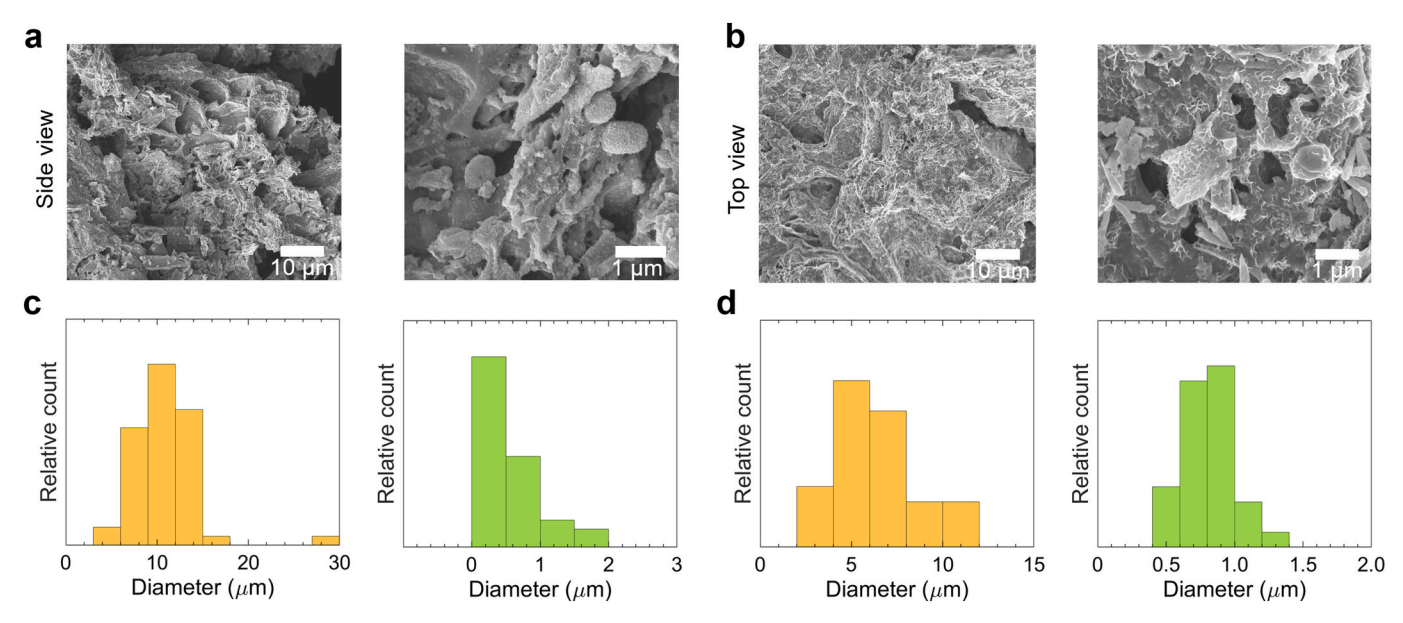


Fig. 3. SEM images. SEM images of the CM (a) side view and (b) top view. Channel size distribution of (c) side view and (d) top view.

Y. Tian et al. Desalination 520 (2021) 115345

evaporation rate is to efficiently absorb the solar irradiance. Attributed to the black carbon constitute existing in carbonized manure and the hierarchically porous structures of the CM evaporator, the black carbon efficiently absorber the sunlight while the hierarchically porous structures of the CM evaporator elongate the optical path to enhance the solar absorptance. The incident sunlight is barely reflected due to the nanoscale light-trapping after multireflection and scatteration of the carbon fiber networks. The surface of the CM evaporator shows a broadband solar absorptance of about 0.98 for the AM 1.5 solar spectrum (Figs. 4a and S4). It is much higher than that of the uncarbonized manure, which mainly consists of cellulose and lignin, possessing a solar absorptance value of 0.77. The main constituents of the uncarbonized manure are cellulose while CM mainly consists of carbon. The large difference of solar absorptance between uncarbonized manure and CM is mainly attributed to the high extinction coefficient of carbon compared with the negligible extinction coefficient of cellulose (Fig. S5). The high extinction coefficient of carbon renders it becoming an efficient photothermal material which is highly desired in solar-driven desalination. Moreover, the solar absorptance is enhanced by scattering effects when carbon fibers are in nanoscale. High scattering efficiency means that the income sunlight can be efficiently absorbed by the carbon fibers. The shape of carbon fiber in the CM evaporator is not in a regular geometry. To investigate the geometry and size effect of carbon fibers on the scattering efficiency, the FDTD technique is employed to simulate the scattering efficiency spectra of carbon fibers in various geometries and different characteristic sizes (Figs. S6-S8). The cross-section of individual carbon fiber is in irregular geometries (Figs. 3a,b, S2 and S3), four cross-section shapes of square, triangular, circle, and hexagon are used to simplify the FDTD simulation. The geometries of cross-section have no significant effects on the scattering efficiency with a characteristic size of 10 μm (Fig. S7), indicating that irregular shapes of carbon fibers all contribute to the high solar absorptance. The scattering efficiency of carbon fibers with various diameters in a rectangular shape shows that fibers with a diameter of 1 μ m have high scattering effects (Fig. S8) and this is corresponding to the size distribution of top surface for CM evaporator (Fig. 3b,d). Moreover, the solar absorptance of CM is angle-independent due to its rough surface and demonstrates a value of 0.97 even at an incident angle of 60°. This indicates that it can efficiently absorb sunlight even at large angles of incidence (Fig. 4b), attributed to the diffused surface of CM, which is illustrated by the transmittance haze spectrum of the carbon fibers (Fig. 4c). The transmittance haze of carbon fibers is over 0.96 over the solar wavelength regions, elucidating the strong scattering effects of carbon fibers on sunlight (Figs. S6–S8). This feature enables CM to act as an outstanding solar absorber at any time of the day, removing the expensive investment of solar tracking systems.

Water absorption is another key factor for fast solar evaporation since sufficient water needed to be pumped upward to make up for the loss of evaporation. The dynamic water contact angle of CM elucidates a 0° contact angle, indicating the superhydrophilicity of the CM surface and its quick water absorption capabilities, as the waterdrop disappears instantly after contact with the CM surface (Fig. 4d). The high-speed camera images demonstrate that the waterdrop only stands for 1.1 ms on the CM surface before being fully absorbed (Fig. 4e). The dynamic contact angle measurement and high-speed camera images demonstrate the quick water absorption capability of the CM evaporator that can facilitate its fast water uptake during the evaporation process. The water absorption ratio of the CM evaporation determines its long-time evaporation stability. Water absorption ratio curves of CM elucidate the enhanced water absorption capacity of CM as compared with uncarbonized manure (Fig. 4f). The final water absorption ratio of CM reaches up to 4.5 g g^{-1} , which is approximately twice that of the uncarbonized manure. Additionally, the stabilized water absorption time of CM is about 20 min, which is much shorter than that of the uncarbonized manure (60 min). This is because the porosity of CM is much higher than that of the uncarbonized manure (Fig. S9). Despite the strong water absorption abilities of the CM, its thermal conductivity in the wet state $(0.10~\mathrm{W}~\mathrm{m}^{-1}~\mathrm{K}^{-1})$ does not increase significantly compared with its dry state (0.15 W m⁻¹ K⁻¹), as shown in Fig. 4g. This ensures that the CM can efficiently localize heat within the interfacial evaporation region during the desalination process.

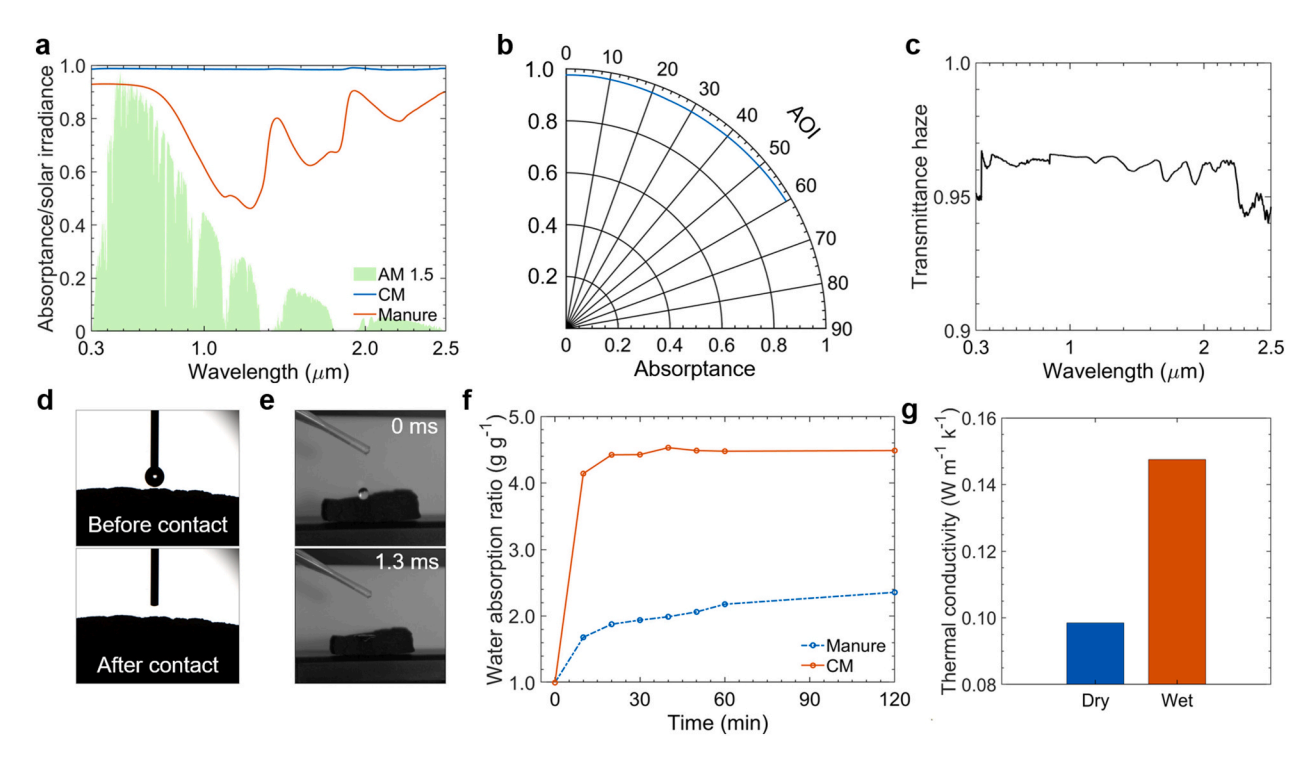


Fig. 4. Optical properties, water absorption, and thermal conductivity of the CM. (a) The solar absorptance spectrum of the soaked CM and wet manure exhibiting against the normalized AM 1.5 solar irradiance (ASTM G173). (b) The overall solar absorptance of the CM under various angles of incidence (AOI). (c) Transmittance haze of the carbon fibers of CM. (d) The dynamic water contact angle of the CM. (e) Rapid water absorption demonstrations of the CM under a high-speed camera. (f) Water absorption ratio of the dry manure and the CM. (g) Thermal conductivity of the dry CM and the soaked CM.

Y. Tian et al. Desalination 520 (2021) 115345

3.3. Photothermal response and solar desalination performance of the CM evaporator

The photothermal response of the CM evaporator is characterized by the infrared (IR) camera. Fig. S10 elucidates the temperature distribution of the pure water and the CM evaporator under 1 sun irradiance. The water surface temperature rises from 20.2 °C to 32.6 °C within 50 min, while the CM evaporator surface temperature increases from 22.9 °C to 47.9 °C within the same period. This illustrates the excellent heat localization capability of the CM evaporation device. For the first 10 min, the CM evaporator experiences a temperature increase of 15.2 °C, which is much higher than that of pure water. This rapid fast photothermal response shortens the warm-up time for an evaporation system, enhancing the freshwater yield rate. For a practical outdoor environment, solar intensities vary at different times of the day and different months of the year, most notably due to varying cloud coverage and winter months, respectively. To demonstrate the photothermal response under various solar intensities, we further study the temperature responses of CM evaporator under 0.6, 0.8, and 1.3 kW m⁻² (Fig. 5a). The stabilized surface temperature of the CM evaporator increases from 39.4 °C to 53.4 °C when the solar intensity is raised from 0.6 kW m^{-2} to 1.3 kW m^{-2} . Moreover, the time required to reach a stable maximum surface temperature for the CM evaporator reduces from 39 min for 0.6 suns to 30 min for 1.3 suns, respectively.

The solar desalination performance of the CM evaporation device is characterized by monitoring the mass change using different salt concentrations (Figs. 5b and S11a). Different salinities NaCl solutions are employed to simulate various brine salinities. All the mass measurements are conducted 30 min after the solar simulator begins illuminating the experimental setup. The evaporation rate decreases from 2.36 kg m $^{-2}$ h $^{-1}$ to 2.02 kg m $^{-2}$ h $^{-1}$ when the salt concentration increases from 10 wt% to 20 wt%, which is much higher than previously reported results [42,43,44,40]. When the salinity of the NaCl solution reaches 25 wt%, salt crystals are visible on the top surface of the CM

evaporator after a 1.5 h experiment. Despite this, the CM evaporator still yields an evaporation rate of 1.96 kg m⁻² h⁻¹ under these conditions. The desalination performance under various solar intensities is also evaluated to illustrate the working effectiveness under diverse weather conditions (Fig. 5c). Our proposed CM evaporation device has an evaporation rate of 1.59 kg m⁻² h⁻¹ under 0.6 suns, which exemplifies its efficient working performance under weak sunlight. This is attributed to the excellent heat localization of CM, PS foam, and the cotton wipe (Fig. S12). When the solar intensity is 1.3 kW m^{-2} , the evaporation rate is enhanced to 2.70 kg m⁻² h⁻¹ without any salt crystallization occurring on the CM evaporator surface. As demonstrated above, the evaporation rate of the CM evaporator (2.25 kg m⁻² h⁻¹) is much larger than the theoretical limit (1.51 kg m $^{-2}$ h $^{-1}$) under 1 sun (Supplementary note). This high efficiency mainly results from the expanded evaporation surface, elucidated by the surface topography of the CM (Fig. 5d). The numerous peaks and valleys dramatically enlarge the effective surface areas where interfacial evaporation takes place. This enlarged evaporation interface yields similar effects to that of a reduced evaporation enthalpy, strongly favor efficient evaporation performance. To validate this, the continuous evaporation rate measurement of CM and pure water is conducted in a dark environment for 6 h. This dark environment eliminates all sunlight effects and ensures that evaporation occurs without the driving force from the sunlight (Fig. 5e). The calculated evaporation rate and equivalent enthalpy of CM evaporator and pure water are shown in Fig. S13. The dark environment evaporation rate of CM evaporator (70.0 g m⁻² h⁻¹) is much higher than that of the pure water (39.1 g m $^{-2}$ h $^{-1}$), and the equivalent enthalpy of the CM evaporator (1329.8 kJ kg⁻²) is much lower than that of the pure water (2386.7 kJ kg⁻²), due to the expanded evaporation areas of the CM surface. Differential scanning calorimetric (DSC) characterization shows the reduced evaporation enthalpy of water in the CM evaporator. A sharp signal peak is observed at 100 °C and then decreases dramatically, indicating the water evaporates immediately and completely (Fig. 5f). The peaks of CM soaked with water are broader than that of pure water.

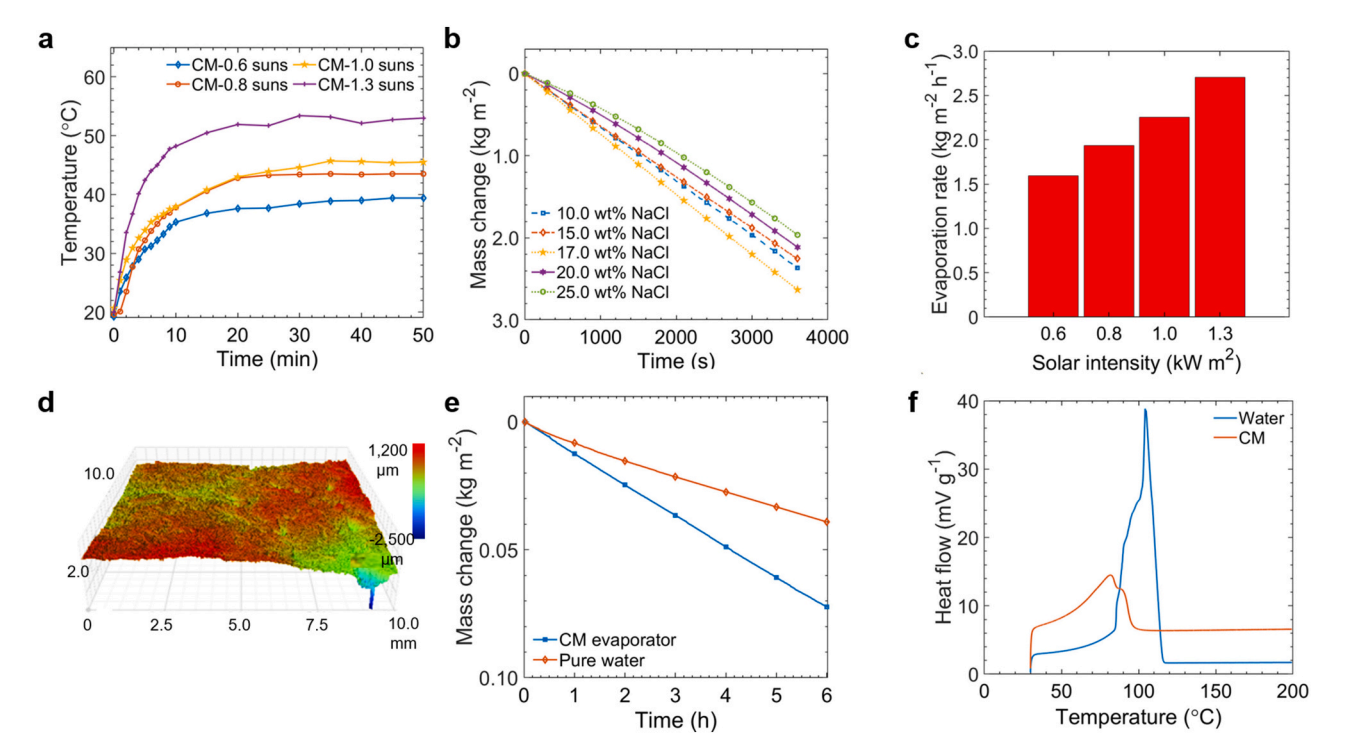


Fig. 5. Solar desalination evaluation of the CM. (a) Temperature evolutions of the bulk brine without the evaporator and the CM under various solar intensities. (b) Mass changes of the CM using NaCl solutions with different salinities. (c) Evaporation rate of the CM using the 15 wt% NaCl solution under different solar intensities. (d) The topography of the CM, exhibiting its increased evaporation area. (e) Evaporation rate of the CM and pure water in a dark environment. (f) DSC thermograms of CM and pure water.

This demonstrates that the evaporation enthalpy of water in CM is reduced because the specific evaporation area of CM is expanded by the carbonization process.

3.4. Salt self-cleaning ability and stability of CM evaporator

To test the long-term stability of evaporation performance for the CM evaporator, the CM evaporator is placed in a 15 wt% NaCl solution and taken it out after 1, 3, 7, 14, and 21 days to repeat the solar desalination experiment. It is demonstrated that the evaporation rate fluctuates around 2.2 kg m⁻² h⁻¹ without significant degradation after long-time exposure to a high-salinity brine, which is highly desirable for real-life engineering applications (Fig. 6a). This reveals the working stability and robustness of the CM evaporator in the high-salinity brine. The durability of the solar absorptance is another key aspect for the CM evaporator to working in high salinity conditions. The solar absorptance spectra of CM evaporator after immersion into a 15 wt% NaCl for 21 days shows no obvious degradation (Fig. 6b). The minor differences between the original CM and immersed CM evaporator are attributed to small measurement errors and the remaining salt present on the surface of CM. Moreover, the FTIR transmittance spectra of the original CM and the immersed CM are consistent for most of the absorption peaks besides those of the O-H stretching vibration peaks at \sim 3400 cm⁻¹ (Fig. 6c). The O-H stretching vibration peaks of the immersed CM may come from the small amount of residual H2O introduced by the long-term immersion even though the CM is baked for 1 h before FTIR transmittance measurement.

Water quality is another factor critical to the evaluation of the performance of solar-driven interfacial desalination devices. The salinity of the 15 wt% NaCl solution and the collected water is evaluated (Fig. 6d). It is revealed that the salinity of the 15 wt% brine sample is significantly reduced by about four orders of magnitude through the desalination process, achieving a final salinity that is two orders of magnitude below the freshwater standards defined by the World Health Organization (WHO, 1) and the US Environmental Protection Agency (EPA, 0.5),

respectively.

To evaluate the excellent salt self-cleaning capability of the CM evaporator, simulated salt accumulation and salt self-cleaning process on the evaporator top surface was conducted under concentrated solar irradiance with a high-salinity water supply (15% NaCl solution). The experimental setup includes a solar simulator as the light source, a Fresnel lens to concentrate sunlight into high flux, a lifting platform for adjusting the distance between the top surface of the CM evaporator and the Fresnel lens (Fig. 6e). The 15 wt% NaCl solution was employed as the water source to accelerate the salt accumulation process. A solar intensity of 19 kW m⁻² irradiated on the surface of the CM evaporator for 60 min, during which the focused sunlight heated the top surface of the CM evaporator, and water continuously evaporated, making the salinity of remaining water increase in a short time. Then, the salt crystals are gradually formed and accumulated on the surface of the CM evaporator. Salt blockage of the pores within the CM evaporator happens when the evaporation rate and the salinity of the bulk water are high. The salt residual cannot be efficiently rejected to the underlying bulk water because the salt concentration difference between the evaporation surface and underlying bulk water becomes smaller, even the higher concentration appears on the top surface as the evaporation progresses. Salt crystals gradually accumulated on the top surface (Fig. 6f). Generally, the CM evaporator cannot be blocked by the salt crystals due to its porous structure and efficient water supply to drive the salt down to the bulk water. However, under the situations of concentrated sunlight and high-salinity water, more salts need to be dissipated from the evaporation surface that is more than the salt rejection capability of the CM evaporator. The salt crystal blocks the pores of the CM evaporator, then the driven force from the capillary phenomena becomes weak, and the underlying low-salinity water cannot be pumped up to dissolve the salt residual.

After 60 min, salt crystals covered most of the top surface of the CM evaporator. Then the solar simulator was shut down, the CM evaporator was placed on top of the PVC foam and was connected with a new 15 wt % NaCl solution through a cotton wipe since the concentration of the old

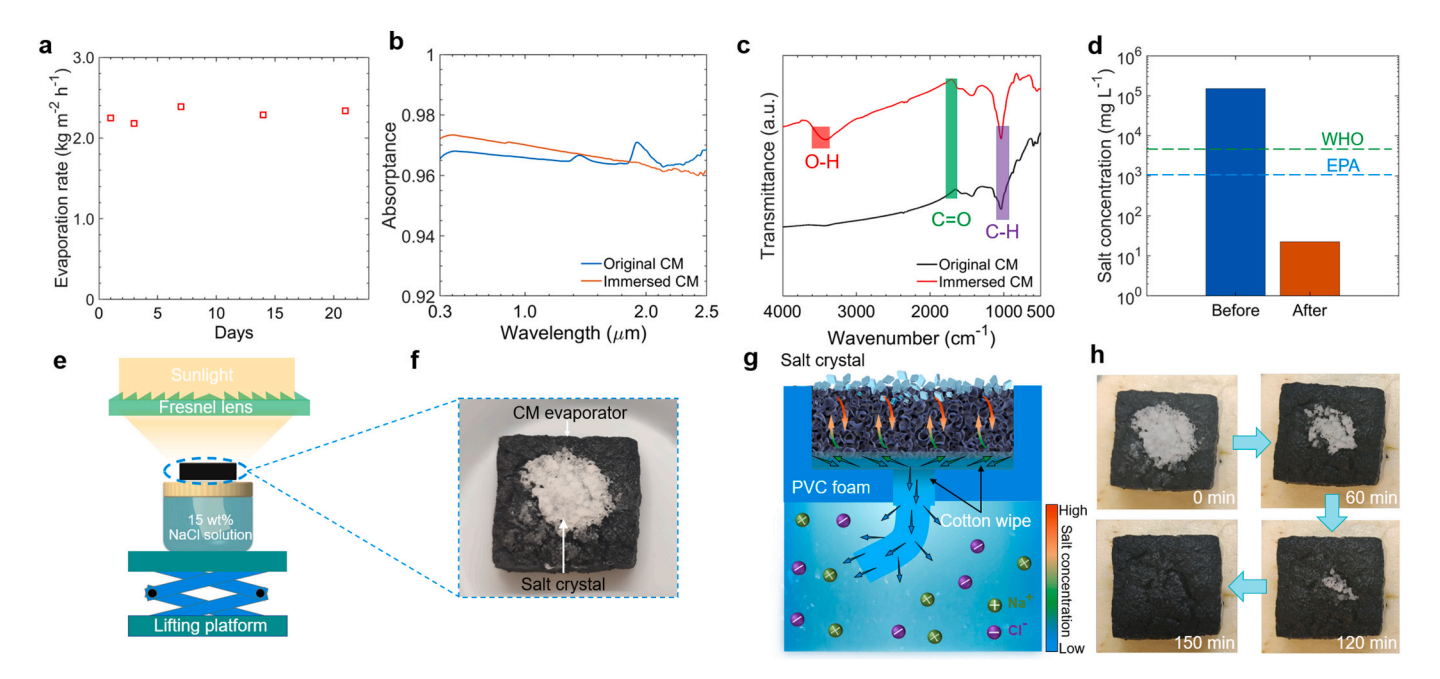


Fig. 6. Evaporated water quality, robustness, and salt rejection of the CM. (a) Long-term desalination performance of the CM after being immersed into the 15 wt% NaCl solution for 1, 3, 7, 14, and 21 days. (b) Solar absorptance spectra and (c) FTIR transmittance spectra of the original CM and CM evaporator after being immersed in a 15 wt% NaCl solution for 21 days. (d) The salinity of the brine water before and after desalination. (e) Schematic illustrating the experimental setup of salt accumulation under concentrated sunlight. (f) Top view showing the accumulated salt on the top surface of the CM evaporator after 30 min with 15 wt% NaCl solution as the water supply. (g) Schematic elucidating the working process of the salt rejection for CM evaporator with the 15 wt% NaCl solution. (h) Time-lapse photographs of the salt dissolving process on the top surface of the CM evaporator.

NaCl solution increased after 60 min fast evaporation under concentrated solar intensity (Fig. 6g). Without the strong solar intensity input, strong evaporation is extinguished. The accumulated salt crystals started to dissolve and the salt concentration gradient from the upper surface to the lower region of the CM evaporator drives the salt down to the underlying bulk water through the water path of interconnected porous structures and the cotton wipe to the underlying 15 wt% NaCl solution. The dissolving process of the accumulated salt crystals on the top surface was recorded and shown as time-lapse images in Fig. 6h. About half of the slat crystals disappear within the first 60 min which elucidated the quick salt self-cleaning ability of the CM evaporator. All the accumulated salt dissolves in 150 min after the solar simulator was off, showing the salt self-cleaning performance of the CM evaporator. The excellent salt self-cleaning capability of the bimodal CM evaporator using the 15 wt% brine can be attributed mainly to two factors. Firstly, the NaCl crystals quickly dissolve after fast evaporation is down and form a saturated NaCl solution within the small upper regions of the CM evaporator. The concentration gradient between the saturated region and other regions with the unsaturated NaCl solution provides the driving force for salt drainage to the relatively low concentration brine below. Second, the micro-sized channels offer a pathway for the high concentration brine to flow down to the bulk brine via both diffusion and convection, while the nano-sized channels pump brine up to dissolve the salt crystals.

4. Conclusions

In summary, the carbonized manure based photothermal evaporator has been demonstrated a fast evaporation rate of 2.25 kg m $^{-2}$ h $^{-1}$ under 1 sun irradiance (1 kW m^{-2}) using a 15 wt% NaCl solution. It also shows continuous and excellent desalination performance in higher salinity of up to 25 wt%. The porous structure of the carbonized manure evaporator enhances the light trapping effect and endures a high solar absorptance of 0.98 for efficient photothermal conversion. While the nano-sized channels are less suited for salt rejection, they offer efficient nanoscale light trapping through multiple reflections and scatterations that occur within the channels. The strong capillary force within these pores helps to uptake water effectively to the top evaporation surface. The hierarchical porous structure of the carbonized manure evaporator is essential for salt drainage in high-salinity brines. The micro-sized channels are extremely beneficial for the diffusion of partially evaporated high-concentration brine to the bulk brine. Moreover, the microsized channels do not sacrifice significantly the heat localization capability due to the nanoscale channel matrix that reduces the thermal conductivity of the CM evaporator. Overall, a balance in the amount of the nano- and micro-sized channels yields a CM evaporator with a high solar absorptance, rapid water transportation, excellent heat localization, and efficient salt rejection. The naturally existing bimodal structure appearing after such a simple fabrication method presents strong support for mimicking this structure to develop a similar hierarchical structure with other materials. Such structures can be employed to waste heat-assisted evaporation and enhanced evaporation cooling.

CRediT authorship contribution statement

Yanpei Tian: Conceptualization, Methodology, Validation, Writing. Xiaojie Liu: Methodology, Writing, review and editing. Ziqi Wang: Conceptualization, Methodology, Characterization. Andrew Caratenuto: Characterization, Methodology. Shiyu Zhou: Characterization, Methodology. Fangqi Chen: Characterization, Methodology. Yisheng Wan: Writing, review, and editing. Yi Zheng: Supervision, Writing, review, and editing.

Declaration of competing interest

The authors declare that they have no known competing financial

interests or personal relationships that could have appeared to influence the work reported in this paper.

Acknowledgments

This project is supported by the National Science Foundation through grant number CBET-1941743. The authors would like to thank Blackbird Farm for kindly providing the fresh cattle manure.

Appendix A. Supplementary data

Supplementary data to this article can be found online at https://doi.org/10.1016/j.desal.2021.115345.

References

- J.J. Koh, G.J. Lim, S. Chakraborty, Y. Zhang, S. Liu, X. Zhang, S.C. Tan, Z. Lyu, J. Ding, C. He, Robust, 3d-printed hydratable plastics for effective solar desalination, Nano Energy 79 (2021), 105436.
- [2] K. Liu, W. Zhang, H. Cheng, L. Luo, B. Wang, Z. Mao, X. Sui, X. Feng, A nature-inspired monolithic integrated cellulose aerogel-based evaporator for efficient solar desalination, ACS Appl. Mater. Interfaces 13 (8) (2021) 10612–10622.
- [3] T. Xu, Y. Xu, J. Wang, H. Lu, W. Liu, J. Wang, Sustainable self-cleaning evaporator for long-term solar desalination using gradient structure tailored hydrogel, Chem. Eng. J. 415 (2021), 128893.
- [4] X. Dong, L. Cao, Y. Si, B. Ding, H. Deng, Cellular structured cnts@ sio2 nanofibrous aerogels with vertically aligned vessels for salt-resistant solar desalination, Adv. Mater. 32 (34) (2020) 1908269.
- [5] Z. Xu, L. Zhang, L. Zhao, B. Li, B. Bhatia, C. Wang, K.L. Wilke, Y. Song, O. Labban, J.H. Lienhard, et al., Ultrahigh-efficiency desalination via a thermally-localized multistage solar still, Energy Environ. Sci. 13 (3) (2020) 830–839.
- [6] Q. Wang, F. Jia, A. Huang, Y. Qin, S. Song, Y. Li, M.A.C. Arroyo, Mos2@ sponge with double layer structure for high-efficiency solar desalination, Desalination 481 (2020), 114359.
- [7] Y. Yao, P. Zhang, C. Jiang, R.M. DuChanois, X. Zhang, M. Elimelech, High performance polyester reverse osmosis desalination membrane with chlorine resistance, Nat. Sustain. 4 (2) (2021) 138–146.
- [8] M. Liu, Q. He, Z. Guo, K. Zhang, S. Yu, C. Gao, Composite reverse osmosis membrane with a selective separation layer of double-layer structure for enhanced desalination, anti-fouling and durability properties, Desalination 499 (2021), 114838.
- [9] D. von Eiff, P.W. Wong, Y. Gao, S. Jeong, A.K. An, Technical and economic analysis of an advanced multi-stage flash crystallizer for the treatment of concentrated brine, Desalination 503 (2021), 114925.
- [10] A. Snoussi, N. Chekir, A.B. Brahim, Entropy generation in multi-stage flash desalination plants, international journal of energy and environmental, Engineering (2020) 1–13.
- [11] C. Méndez, Y. Bicer, Integrated system based on solar chimney and wind energy for hybrid desalination via reverse osmosis and multi-stage flash with brine recovery, Sustainable Energy Technol. Assess. 44 (2021), 101080.
- [12] E.J. Okampo, N. Nwulu, Optimisation of renewable energy powered reverse osmosis desalination systems: a state-of-the-art review, Renew. Sust. Energ. Rev. 140 (2021), 110712.
- [13] P.J. Alvarez, C.K. Chan, M. Elimelech, N.J. Halas, D. Villagrán, Emerging opportunities for nanotechnology to enhance water security, Nat. Nanotechnol. 13 (8) (2018) 634–641.
- [14] M. Elimelech, W.A. Phillip, The future of seawater desalination: energy, technology, and the environment, Science 333 (6043) (2011) 712–717.
- [15] X. Chen, N.Y. Yip, Unlocking high-salinity desalination with cascading osmotically mediated reverse osmosis: energy and operating pressure analysis, Environ. Sci. Technol. 52 (4) (2018) 2242–2250.
- [16] P. Tao, G. Ni, C. Song, W. Shang, J. Wu, J. Zhu, G. Chen, T. Deng, Solar-driven interfacial evaporation, Nat. Energy 3 (12) (2018) 1031–1041.
- [17] L. Zhu, M. Gao, C.K.N. Peh, G.W. Ho, Recent progress in solar-driven interfacial water evaporation: advanced designs and applications, Nano Energy 57 (2019) 507–518.
- [18] N. Li, L. Qiao, J. He, S. Wang, L. Yu, P. Murto, X. Li, X. Xu, Solar-driven interfacial evaporation and self-powered water wave detection based on an all-cellulose monolithic design, Adv. Funct. Mater. 31 (7) (2021) 2008681.
- [19] L. Zhang, Z. Xu, L. Zhao, B. Bhatia, Y. Zhong, S. Gong, E.N. Wang, Passive, high-efficiency thermally-localized solar desalination, Energy Environ. Sci. 14 (4) (2021) 1771–1793.
- [20] H.N. Panchal, M. Doshi, P. Chavda, R. Goswami, Effect of cow dung cakes inside basin on heat transfer coefficients and productivity of single basin single slope solar still, Int. J. Appl. Eng. Res. 1 (4) (2010) 675.
- [21] H.N. Panchal, Performance analysis of solar still with cow dung cakes and blue metal stones, Front. Energy 9 (2) (2015) 180–186.
- [22] H. Panchal, D.K. Patel, P. Patel, Theoretical and experimental performance analysis of sandstones and marble pieces as thermal energy storage materials inside solar stills, Int. J. Ambient Energy 39 (3) (2018) 221–229.

- [23] H. Panchal, J. Patel, S. Chaudhary, A comprehensive review of solar cooker with sensible and latent heat storage materials, Int. J. Ambient Energy 40 (3) (2019) 329–334.
- [24] M. Vaka, R. Walvekar, M. Khalid, P. Jagadish, N.M. Mubarak, H. Panchal, Synthesis of hybrid graphene/tio2 nanoparticles based high-temperature quinary salt mixture for energy storage application, J. Energy Storage 31 (2020), 101540.
- [25] M. Patel, C. Patel, H. Panchal, Performance analysis of conventional triple basin solar still with evacuated heat pipes, corrugated sheets and storage materials, Groundw. Sustain. Dev. 11 (2020), 100387.
- [26] C. Shen, Y. Zhu, X. Xiao, X. Xu, X. Chen, G. Xu, Economical salt-resistant superhydrophobic photothermal membrane for highly efficient and stable solar desalination, ACS Appl. Mater. Interfaces 12 (31) (2020) 35142–35151.
- [27] L. Zhu, L. Sun, H. Zhang, H. Aslan, Y. Sun, Y. Huang, F. Rosei, M. Yu, A solution to break the salt barrier for high-rate sustainable solar desalination, Energy Environ. Sci. 14 (4) (2021) 2451–2459.
- [28] N. Cao, S. Lu, R. Yao, C. Liu, Q. Xiong, W. Qin, X. Wu, A self-regenerating air-laid paper wrapped asa 3d cone-shaped janus evaporator for efficient and stable solar desalination, Chem. Eng. J. 397 (2020), 125522.
- [29] J. Lee, K. Kim, S.H. Park, G.Y. Yoon, J. Kim, S.J. Lee, Macroporous photothermal bilayer evaporator for highly efficient and self-cleaning solar desalination, Nano Energy 77 (2020), 105130.
- [30] G. Ni, S.H. Zandavi, S.M. Javid, S.V. Boriskina, T.A. Cooper, G. Chen, A salt-rejecting floating solar still for low-cost desalination, Energy Environ. Sci. 11 (6) (2018) 1510, 1510
- [31] H.M. Qiblawey, F. Banat, Solar thermal desalination technologies, Desalination 220 (1–3) (2008) 633–644.
- [32] F. Wang, Z. Hu, Y. Fan, W. Bai, S. Wu, H. Sun, Z. Zhu, W. Liang, A. Li, Salt-rejection solar absorbers based on porous ionic polymers nanowires for desalination, Macromol. Rapid Commun. 42 (4) (2021) 2000536.
- [33] J. Li, X. Zhou, J. Zhang, C. Liu, F. Wang, Y. Zhao, H. Sun, Z. Zhu, W. Liang, A. Li, Migration crystallization device based on biomass photothermal materials for efficient salt-rejection solar steam generation, ACS Appl. Energy Mater. 3 (3) (2020) 3024–3032.
- [34] Y. Kuang, C. Chen, S. He, E.M. Hitz, Y. Wang, W. Gan, R. Mi, L. Hu, A high-performance self-regenerating solar evaporator for continuous water desalination, Adv. Mater. 31 (23) (2019) 1900498.
- [35] Y. Zhang, T. Xiong, L. Suresh, H. Qu, X. Zhang, Q. Zhang, J. Yang, S.C. Tan, Guaranteeing complete salt rejection by channeling saline water through fluidic photothermal structure toward synergistic zero energy clean water production and in situ energy generation, ACS Energy Lett. 5 (11) (2020) 3397–3404.

- [36] K. Xu, C. Wang, Z. Li, X. Yan, X. Mu, M. Ma, P. Zhang, Architecting a janus biomass carbon/sponge evaporator with salt-rejection and ease of floatation for sustainable solar-driven desalination, Environ. Sci.: Water Res. Technol. 7 (5) (2021) 879–885.
- [37] D. Li, X. Zhang, S. Zhang, D. Wang, Z. Wang, Y. Liu, X. Yu, Q. Zhao, B. Xing, A flexible and salt-rejecting electrospun film-based solar evaporator for economic, stable and efficient solar desalination and wastewater treatment, Chemosphere 267 (2021), 128916.
- [38] L. Wu, Z. Dong, Z. Cai, T. Ganapathy, N.X. Fang, C. Li, C. Yu, Y. Zhang, Y. Song, Highly efficient three-dimensional solar evaporator for high salinity desalination by localized crystallization, Nat. Commun. 11 (1) (2020) 1–12.
- [39] P.-F. Liu, L. Miao, Z. Deng, J. Zhou, Y. Gu, S. Chen, H. Cai, L. Sun, S. Tanemura, Flame-treated and fast-assembled foam system for direct solar steam generation and non-plugging high salinity desalination with self-cleaning effect, Appl. Energy 241 (2019) 652–659.
- [40] S. He, C. Chen, Y. Kuang, R. Mi, Y. Liu, Y. Pei, W. Kong, W. Gan, H. Xie, E. Hitz, et al., Nature-inspired salt resistant bimodal porous solar evaporator for efficient and stable water desalination, Energy Environ. Sci. 12 (5) (2019) 1558–1567.
- [41] Y.-Q. Luo, F. Song, J.-M. Wu, F. Wang, X.-L. Wang, Y.-Z. Wang, A nature-inspired suspended solar evaporator for water desalination of high-salinity brines, Chem. Eng. J. 421 (2021), 129824.
- [42] V. Kashyap, A. Al-Bayati, S.M. Sajadi, P. Irajizad, S.H. Wang, H. Ghasemi, A flexible anti-clogging graphite film for scalable solar desalination by heat localization, J. Mater. Chem. A 5 (29) (2017) 15227–15234.
- [43] W. Xu, X. Hu, S. Zhuang, Y. Wang, X. Li, L. Zhou, S. Zhu, J. Zhu, Flexible and salt resistant janus absorbers by electrospinning for stable and efficient solar desalination, Adv. Energy Mater. 8 (14) (2018) 1702884.
- [44] N. Xu, J. Li, Y. Wang, C. Fang, X. Li, Y. Wang, L. Zhou, B. Zhu, Z. Wu, S. Zhu, et al., A water lily-inspired hierarchical design for stable and efficient solar evaporation of high-salinity brine, Sci. Adv. 5 (7) (2019), eaaw7013.
- [45] S. Cheng, Z. Yu, Z. Lin, L. Li, Y. Li, Z. Mao, A lotus leaf like vertical hierarchical solar vapor generator for stable and efficient evaporation of high-salinity brine, Chem. Eng. J. 401 (2020), 126108.
- [46] X. Chen, Z. Wu, D. Lai, M. Zheng, L. Xu, J. Huo, Z. Chen, B. Yuan, M.-L. Fu, Resilient biomass-derived hydrogel with tailored topography for highly efficient and long-term solar evaporation of high-salinity brine, J. Mater. Chem. A 8 (43) (2020) 22645–22656.
- [47] L. Pandiscia, Haze measurement using a UV-visible spectrophotometer. https://https://https://www.norlab.com/library/application-note/10757. 2019.
- [48] E.D. Palik, Handbook of Optical Constants of Solids Vol. 3, Academic press, 1998.